Article

Local Structure in U(IV) and U(V) Environments: The Case of U_3O_7

Gregory Leinders,* René Bes, Kristina O. Kvashnina, and Marc Verwerft

Read Online

ACCESS | Metrics & More | Article Recommendations | SI Supporting Information

ABSTRACT: A comprehensive analysis of X-ray absorption data obtained at the U L_3-edge for a systematic series of single-valence (UO_2, KUO_3, UO_3) and mixed-valence uranium compounds (U_4O_9, U_3O_7, U_3O_8) is reported. High-energy resolution fluorescence detection (HERFD) X-ray absorption near-edge spectroscopy (XANES) and extended X-ray absorption fine structure (EXAFS) methods were applied to evaluate U(IV) and U(V) environments, and in particular, to investigate the U_3O_7 local structure. We find that the valence state distribution in mixed-valence uranium compounds cannot be confidently quantified from a principal component analysis of the U L_3-edge XANES data. The spectral line broadening, even when applying the HERFD-XANES method, is sensibly higher (~3.9 eV) than the observed chemical shifts (~2.4 eV). Additionally, the white line shape and position are affected not only by the chemical state, but also by crystal field effects, which appear well-resolved in KUO_3. The EXAFS of a phase-pure U_3O_7 sample was assessed based on an average representation of the expanded $U_{60}O_{140}$ structure. Interatomic U−O distances are found mainly to occur at 2.18 (2), 2.33 (1), and 3.33 (5) Å, and can be seen to correspond to the spatial arrangement of cuboctahedral oxygen clusters. The interatomic distances derived from the EXAFS investigation support a mixed U(IV)−U(V) valence character in U_3O_7.
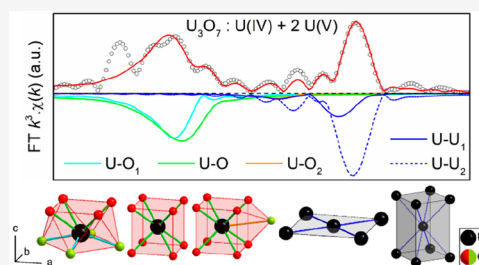
1. INTRODUCTION

The chemical speciation of elements from the actinide series depends mainly on the behavior of electrons in the 5f orbital. In contrast to the role of 4f electrons in the lanthanide series, 5f electrons show a more diverse character and participate in chemical bond formation.[1] A range of possible valence states usually appears in actinide elements, often associated with a complex redox chemistry. The electronic configuration in the ground state of uranium is [Rn] $7s^2$ $6d^1$ $5f^6$, and electronic states associated with $5f^2$, $5f^1$, and $5f^0$ are available, resulting in respectively U(IV), U(V), and U(VI) environments. The binary uranium−oxygen system is remarkably complicated. At temperatures below about 450 °C, two single-valence compounds, uranium(IV) oxide (UO_2) and uranium(VI) oxide (UO_3), and several mixed-valence compounds (U_4O_9, U_3O_7, U_3O_8) occur.[2−4] At more elevated temperatures, a wide phase domain of nonstoichiometric $UO_{2\pm x}$ exists.[5−8] Despite being investigated for almost a century now, the transition and structural relations between the different compounds, especially in the case of U_3O_7, are still not fully understood.

Uranium dioxide has been used as a principal type of nuclear fuel, and remains widely used today.[9] In normal atmospheric conditions, however, the thermodynamically more stable oxide is U_3O_8. Oxidation to U_3O_8 is associated with a considerable reorganization of the crystal structure and results in a volume expansion of about 36%. It is important to understand and predict such transformation, to ensure the safe storage of fresh and irradiated nuclear fuel.[10] The oxidation pathway involves the formation of various intermediate oxides.[11,12] The crystal structure is initially of the fluorite-type, but develops long-

range order due to the incorporation of excess oxygen.[12,13] At the composition O/U = 2.234, an ordered superstructure with cubic symmetry ($U_{256}O_{572}$, but generally referred to as U_4O_9) is encountered.[14] Upon further oxidation, a tetragonal deformation displaying a range of continually changing c/a values sets in, ending at the composition O/U = 2.333.[12,15] This compound, U_3O_7, is the last phase based on a fluorite-type arrangement before the transition to U_3O_8 occurs.[13,16,17]

Identification of U_3O_7 has been ambiguous ever since its first description,[18] with ongoing attempts at modeling the system via theoretical methods.[3,19,20] A comprehensive assessment of perturbations in the local structure was reported first by Jones et al.,[21] following the earlier work of Allen et al. on the application of extended X-ray absorption fine structure (EXAFS) on uranium oxides.[22] They evaluated the contribution of interstitial oxygen atoms to the EXAFS and reported a defect structure based on oxygen vacancies and Willis-type O′ and O″ interstitials.[23] Important progress regarding the description of long-range order, based on experimental results, was made only in recent years.[13,16,17] The general consensus is that, on average, the fluorite-type structure is maintained, and that excess oxygen atoms form clusters which cause local, periodic perturbations of the fluorite structure.

The principal type of defect considered is the cuboctahedral oxygen cluster, i.e., an arrangement of 12 oxygen atoms at the vertices of a cuboctahedron (see Figure 1).[14] The position of
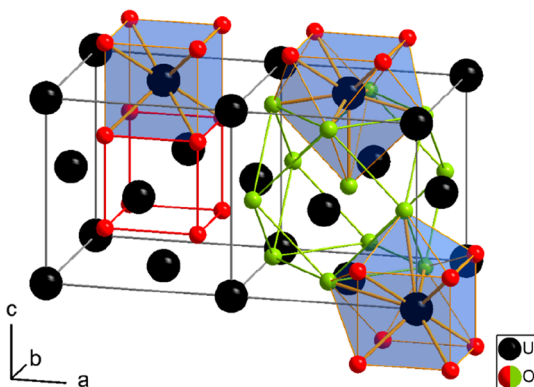
Figure 1. Comparison of the regular anion sublattice in a fluorite-type UO_2 unit cell (left), and the cuboctahedral oxygen cluster in a neighboring unit cell (right). Atoms corresponding to either of the two types of sublattices are colored respectively in red and green to illustrate their geometry. The resulting local uranium environments are shown as blue polyhedra.

the oxygen atoms correspond to the aforementioned Willis O′ interstitials,[23] and hence, are defined at the positions $<uu0>$ from a central octahedral *hole* in the fluorite parent structure. The center of the cuboctahedron is occupied by one additional anion, which is typically displaced along a $<111>$ direction (cf. the Willis O″ interstitial).[24] In a single, fluorite-type unit cell, the cuboctahedral oxygen cluster thus corresponds to the composition U_4O_{13}, as compared to U_4O_8 in the case of a perfect fluorite anion sublattice.

Recently, new insights into the symmetry of the long-range order in U_3O_7 were revealed from room temperature electron diffraction experiments conducted on a sample prepared at thermal equilibrium.[16] On the basis of these results, the spatial distribution of oxygen cuboctahedra which define a structural model ($U_{60}O_{140}$, O/U = 2.333) was found. This superstructure model can be seen to consist of four subcells containing a cuboctahedral oxygen cluster ($4 \times U_4O_{13}$), and 11 subcells with a fluorite-type anion sublattice ($11 \times U_4O_8$). A different structural model ($U_{256}O_{592}$, O/U = 2.313) has been derived from neutron diffraction data obtained during the *in situ* oxidation of UO_2 to U_3O_8.[13] However, inherent to the out-of-equilibrium experimental conditions, the observed structure might have been influenced by the topotactic growth of U_3O_7 onto U_4O_9 when these phases coexist. This can explain also why the superstructure model had a stoichiometry below the nominal 2.333 value, unlike the model derived from a sample in thermal equilibrium.[16]

The occurrence of oxygen clusters in the U_3O_7 structure results in a variety of uranium environments. Some possibilities are displayed in Figure 1; however, their exact nature depends on the size and geometry of the clusters, and their spatial distribution from each other. On average, the uranium valence equals 4.67 to compensate for the negative charge associated with the anion content in U_3O_7, which involves the occurrence of either $1 \times U(IV) + 2 \times U(V)$, or $2 \times U(IV) + 1 \times U(VI)$ local uranium environments. To investigate the exact nature of the charge compensation mechanism in U_3O_7, the use of X-ray absorption near-edge spectroscopy (XANES) has been most

notable. Kvashnina et al. demonstrated the increased sensitivity of high-energy resolution fluorescence detection (HERFD)-XANES to probe chemical shifts at the U M_4-edge, as compared to the U L_3-edge.[2] Using the former technique, a 36 ± 3% U(IV) and 64 ± 3% U(V) character was determined in U_3O_7, resulting in an average valence of 4.64 ± 0.03, which corresponds very well to the nominal value of 4.67.[25] In contrast, according to results obtained from total reflection X-ray fluorescence (TXRF)-XANES at the U L_3-edge, a distribution of $2 \times U(IV) + 1 \times U(VI)$ was found to be marginally favorable over the alternative.[26] However, recent calculations have also reproduced the $1 \times U(IV) + 2 \times U(V)$ distribution in U_3O_7,[27,28] as determined from the U M_4-edge data.[25]

In the current work, the remaining ambiguity concerning the valence distribution in U_3O_7 is finally resolved by discussing new HERFD-XANES data, and additionally, by evaluating the EXAFS. A comprehensive analysis of U(IV) and U(V) environments in single-valence reference samples (UO_2 and KUO_3) is first performed, before investigating the local structure in the more complicated U_3O_7 structure. New insights in the defect structure are obtained.

2. EXPERIMENTAL SECTION

2.1. Sample Preparation. Depleted UO_{2+x} powder supplied by FBFC International (Dessel, Belgium), and having a nuclear-grade impurity content,[29] was used to prepare all samples. A Carbolite TZF1800 tube furnace capable to be used with a variety of dry (dew point < −80 °C) and high-purity (99.9992%) gases was used to perform simple heat treatments. The as-supplied UO_{2+x} powder was first treated at 700 °C under a flow of Ar/5 vol % H_2 to reduce any higher oxide impurity phase to UO_2. Part of this product was then subjected to a treatment at 200 °C under mildly oxidizing conditions (Ar/0.01 vol % O_2) to produce U_4O_9, while another part was treated at 500 °C under oxidizing conditions (N_2/21 vol % O_2) to produce U_3O_8. KUO_3 was subsequently prepared by first mixing stoichiometric amounts of U_3O_8 and K_2CO_3 (Sigma-Aldrich, Belgium) powders followed by annealing at 800 °C under reducing conditions (−400 kJ mol^{-1}).

A simultaneous thermal analyzer (Netzsch STA 449 *F1* Jupiter) was used for synthesis of the more delicate sample materials such as $UO_{2.0}$ and β-UO_3. To lower the susceptibility toward unwanted oxidation,[30] the reduction treatment on the UO_2 powder was repeated at a higher temperature of 900 °C, which results also in a decrease of the specific surface area. After being cooled to room temperature, the STA was flushed first with pure Ar, and then with Ar containing about 80 ppm of O_2 to gently expose the powder to mildly oxidizing conditions. On the basis of the minute mass change that occurred, the final O/U of the sample was evaluated as 2.01 ± 0.01. β-UO_3 was prepared[25] by calcination of previously prepared[25] ammonium diuranate at 540 °C for 30 min, followed by cooling (10 K min^{-1}) to room temperature. Phase purity of all samples was confirmed via X-ray diffraction (the U_3O_7 sample was prepared *in situ* during a nonambient XRD measurement, see section 3.1).

All sample powders (30−50 mg) were intimately mixed with boron nitride powder, inserted into polypropylene sample holders dedicated to cryostat operation at beamline BM20 of the European Synchrotron Radiation Facility (ESRF), and sealed with Kapton foil. In-between the prior synthesis steps and after filling of the sample holders, all samples were transferred into a desiccator to reduce possible interaction with the normal atmosphere.

2.2. Nonambient X-ray Diffraction. *In-situ* X-ray diffraction was performed with a PANalytical X'Pert Pro diffractometer in parafocusing geometry ($\theta-\theta$ configuration), equipped with a Bühler HDK 2.4 nonambient chamber. The radiation source was an LFF Cu X-ray tube (Cu $K\alpha_1$ = 1.5405929 Å),[31] and the detector was a position-sensitive 1D detector operating in scanning mode with an

active length of 2.122° (2θ) and using a front-mounted Ni filter to remove Cu Kβ contribution. A fixed divergence slit (1/2°) and 0.02 rad Soller slit assemblies in combination with a copper beam mask were used to limit the beam divergence.

Specimen preparation consisted in top-loading UO$_2$ powder into a dedicated AlN holder, which slides over the heating strip (Pt/Rh alloy) of the chamber. A type B thermocouple was subsequently inserted in a foreseen recess of the holder, and used to control the sample temperature ($\pm$5 °C above 100 °C). The chamber was sealed and flushed with a constant flow of He/0.5 vol % O$_2$. The sample stage was mechanically aligned before the start of the experiment, and thermal expansion of the heating strip was compensated for via a spring mechanism attached to the strip clamps.

Room temperature (RT) scans were performed over the range 20–121° (2θ) using a step size of 0.008° (2θ). Nonambient scans were optimized to the 31–35° (2θ) range with a step size of 0.017° (2θ) to allow fast data acquisition (5 min per scan). The heating profile consisted of a stepwise heating (20 K min^{-1} with intermediate steps at 50, 100, 150, 200, 225 °C) from room temperature to the target temperature of 250 °C. At each isotherm, after a 5 min hold time, one nonambient scan was performed. At the target temperature of 250 °C the nonambient scan was repeated over 150 times, resulting in a total exposure of 14.5 h. After cooling down to room temperature (40 K min^{-1}) and a 20 min hold time, one final RT scan was performed. The PANalytical Highscore Plus (v4.7) software was used to analyze the X-ray diffraction data.

2.3. X-ray Absorption Spectroscopy. U L_3-edge XANES measurements were performed at BM20 (The Rossendorf Beamline) of the ESRF. The incident energy was scanned between 16.966 and 18.400 keV, using a Si(111) monochromator. HERFD-XANES spectra were measured using an X-ray emission spectrometer equipped with one Si(220) crystal analyzer with 0.5 m bending radius,[32] and a silicon drift X-ray detector in a vertical Rowland geometry.[33] The spectrometer was tuned to the maximum of the U Lα_1 (2p$_{3/2}$ → 3d$_{5/2}$ at 13.614 keV) X-ray emission line using the 880 reflection at a Bragg angle of 72°. The detected intensity was normalized to the incident flux. Beam size was estimated to be 200 μm (vertically) by 450 μm (horizontally). The beamline settings available at the time of the measurements did not allow to achieve ultrahigh energy resolution in HERFD mode. Nevertheless, the total experimental energy broadening (incident energy convoluted with emitted energy and core-hole lifetime broadening) of 3.9 eV was still below the core-hole lifetime broadening of the U L_3-edge ($\sim$8.2 eV). The resolution can be further improved by using a Se(311) crystal monochromator, a Ge(777) crystal analyzer with 1 m bending radius, and by reducing the beamsize below 100 μm.[34]

U L_3-edge EXAFS measurements were also performed at the BM20 beamline of the ESRF, using a closed-cycle helium cryostat operating at 18 K in order to reduce contribution of thermal atomic displacements to the EXAFS signal. The spectra were measured in transmission mode, using 30 cm long ionization chambers running at 1200 V. The detected intensity was normalized to the incident flux, and online energy calibration was available through the Y K-edge excitation energy (17.038 keV) of a metallic yttrium foil placed in the beam path. The total experimental energy broadening (incident energy convoluted with core-hole lifetime broadening) was evaluated at 8.8 eV.

The X-ray absorption spectra were treated using the ATHENA software available in the DEMETER package.[35] Normalization and background removal were performed with linear functions, and the energy threshold value (E_0) was selected at the first inflection point, utilizing the first derivative function. The EXAFS $\chi(k)$ could be extracted up to 18 Å^{-1} and were Fourier-transformed in k space. The contribution of the very high k oscillations on the Fourier-transform was then evaluated to determine a meaningful k-range, which led to a restriction using a Hann window of $3 < k < 15$–16 Å^{-1} for the various samples. EXAFS data fitting was subsequently performed using the ARTEMIS software of DEMETER, and the *ab initio* code FEFF 8.40 was used to calculate phases and amplitudes for the interatomic scattering paths,[36] based on the provided crystallographic information

of the various compounds. The global parameters consisted of the scattering factor (S_0^2) and the shift in threshold energy (ΔE_0). A description of the structural models and the parameter set used to fit individual scattering paths is worked out in detail in sections 3.3 and 3.4.

3. RESULTS

3.1. *In-Situ* Oxidation of UO$_2$ to U$_3$O$_7$. In order to study the structural evolution of the U$_3$O$_7$ phase following oxidation of UO$_2$, XRD was performed under nonambient conditions. The scans were restricted to the range 31–35° (2θ), to focus on the transition from cubic UO$_2$ (200) to U$_4$O$_9$ (200)$_p$ reflections, and finally to tetragonally split U$_3$O$_7$ (002)$_p$ and (200)$_p$ reflections. Figure 2 presents a contour plot of the
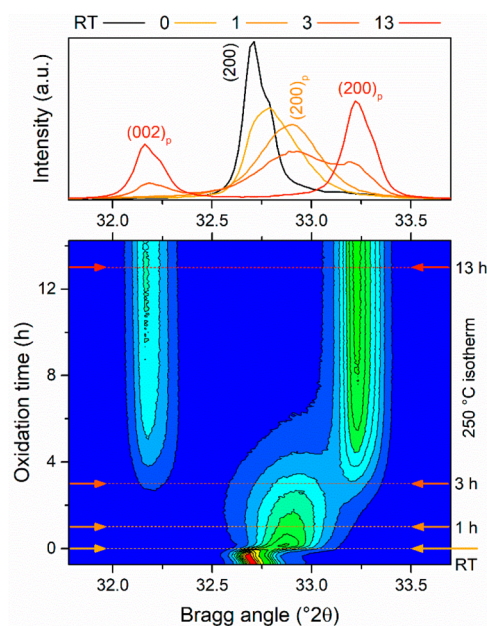
Figure 2. (Bottom) Contour plot of nonambient X-ray diffractograms measured under oxidizing conditions during ramping from room temperature (RT) to 250 °C (denoted as 0 h) and then kept isothermal for 14 h. (Top) XRD patterns measured at various oxidation times; the respective scans are indicated on the contour plot. A transition from UO$_2$ (200) via U$_4$O$_9$ (200)$_p$ to the (002)$_p$ and (200)$_p$ reflections of U$_3$O$_7$ can be observed, occurring respectively at 32.71, 32.88, 32.16, and 33.23° (2θ).

diffracted intensity (respectively blue → green → yellow → red with higher intensity) as a function of diffraction angle and oxidation time at the 250 °C isotherm. A selection of scans measured at different oxidation times is reproduced at the top of the graph.

During heating from room temperature (RT) to about 150 °C one observes only a shift in the UO$_2$ (200) reflection from 32.71 to 32.67° (2θ), due to thermal expansion. At increasingly higher temperatures, a broadening on the high angle side occurs, corresponding to evolution of the U$_4$O$_9$ (200)$_p$ reflection around 32.88° (2θ). As the remaining UO$_2$ fraction decreases, eventually (between 1–3 h at 250 °C) a distinct U$_4$O$_9$ peak becomes visible. After 3 h of oxidation, the tetragonal deformation associated with U$_3$O$_7$ sets in, and as time continues a slight evolution in the exact position of the (002)$_p$ and (200)$_p$ reflections can be observed.

The nonambient measurement was completed with a full scan on the U$_3$O$_7$ product, after cooling to room temperature.

Rietveld refinement of the diffraction data was performed, using the crystallographic information on the U_3O_7 parent structure as reported by Leinders et al.[16] The oxygen site occupancy factors (o_f and o_c referred to in ref [16]) were assumed as 0.733 and 0.067, respectively. This follows from the assessment of the U_3O_7 superstructure, which consists of 11 subcells containing fluorite-type oxygen positions and 4 subcells containing cuboctahedral oxygen clusters. Taking the multiplicity of the atomic positions into account, the above values result in an average O/U of 2.333 for the parent structure unit cell. Using this model structure, the refinement converged with very good agreement, and in addition to the lattice constants and peak profile parameters, isotropic temperature factors for the U and O atoms were refined. For simplicity and because X-ray diffraction is not very sensitive to light elements, all B_{iso} O values were constrained to be equal. Results are reported in Table 1.

Table 1. Results from Rietveld Refinement of Room Temperature XRD Data Measured after Completion of the Non-Ambient Program[a]

	U_3O_7 (p)
a_p (pm)	537.93(1)
c_p (pm)	555.22(1)
$B_{iso}U$ (Å^2)	0.35(1)
B_{iso} all O (Å^2)	0.5(1)
R_{wp}	0.077
g.o.f.	1.406

[a]Data measured over the range 20−121° (2θ).

3.2. Evaluation of Chemical States. The XANES spectrum of U_3O_7 was measured at the U L_3-edge using an X-ray emission spectrometer in HERFD mode at ambient conditions, as described in the Experimental Section. The measurement was part of a systematic series on single-valence (UO_2, UO_3) and mixed-valence compounds (U_4O_9, U_3O_8). To probe also a single pentavalent uranium state, the ternary KUO_3 phase was analyzed. In Figure 3, a comparison is made with spectra measured in transmission mode under cryogenic conditions (T = 18 K), optimized for high-quality EXAFS collection. The uranium valence assigned to the different compounds was based on results from a previous study at the U M_4-edge.[25] In general, the shape and width of the white line, and some postedge features are more emphasized in the HERFD-XANES spectra when compared to the standard XANES detection mode. Additionally, in the KUO_3 spectrum, a shoulder on the white line originating from crystal field splitting of U 6d states becomes well-resolved.[34,37] The smaller experimental energy broadening of HERFD-XANES (~3.9 eV) as compared to conventional XANES (~8.8 eV) is also clearly visible in the UO_3 spectrum. The shift in the white line position between UO_2 and UO_3 amounts to 2.4 eV.

An iterative target test (ITT) protocol for principal component analysis of spectra, available in the iterative transformation analysis code (ITFA) developed by Rossberg et al.,[38] was used to evaluate quantitatively the uranium valence state in the mixed-valence compounds. The method parameters were chosen identical to those used in a recent XANES study at the U M_4-edge on the same materials,[25] but with the incident energy range adapted to the corresponding U L_3-edge values (i.e., between 17150 and 17200 eV). On the basis of the transmission XANES data, the ITT did not yield
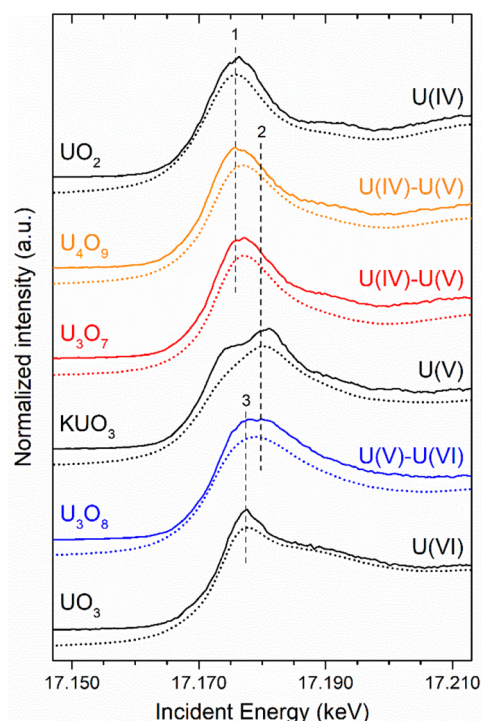
Figure 3. XANES spectra measured at the U L_3-edge in two different modes: (solid line) HERFD-XANES mode using the X-ray emission spectrometer, (dotted line) XANES region from EXAFS scans collected in transmission mode. Vertical dashed lines marked (1), (2), and (3) denote the position of the white line corresponding qualitatively to isolated U(IV)−U(V)−U(VI) components, as derived from the iterative target test excluding KUO_3.

physically meaningful results (e.g., negative contributions of individual components). This can be understood knowing that the expected chemical shifts are around 2.4 eV, whereas the spectral line broadening of the method is much larger (~8.8 eV). In contrast, physically valid results could be obtained by using the HERFD-XANES data. The quantitative distribution, however, is considerably different from the results derived from U M_4-edge spectra;[25] see Table 2. On the basis of the U L_3-edge XANES data set, a considerable contribution of U(VI) would be attributed to all compounds.

It must be recognized that U L_3-edge XANES spectra are not ideal for determining the valence state in actinide materials. According to the dipole selection rules, XANES spectra at the U L_3-edge (excitation from the $2p_{3/2}$ core level) contain information on the unoccupied U 6d states, whereas the oxidation states depend more on the number of U 5f electrons. Hence, the energy shift of the U L_3-edge white line depends also on the redistribution of 6d states with respect to varying crystallographic structures, i.e., crystal field splitting.[34,39,40] In addition to crystal field effects, a quadrupolar electronic transition (2p → 5f) has been reported at the U L_3-edge.[41] Because of the strong correlation between 5f electrons and the uranium chemical state, the quadrupolar transition also affects the overall shape and position of the edge.

Most of the materials selected in the current study are binary uranium oxides having a close crystallographic relation to the fluorite structure,[12] and under the applied conditions (U $L\alpha_1$ emission line) the crystal field splitting does not appear resolved in the XANES spectra.[34] However, in the case of KUO_3 which is an alkali-metal uranate in a perovskite

Table 2. Relative Abundance of Uranium Oxidation States in Mixed-Valence Compounds, Quantified Using ITT on HERFD-XANES Data[a]

	U L_3-edge, incl. KUO_3 (%)				U L_3-edge, excl. KUO_3 (%)				U M_4-edge, ref 25 (%)[25]				
	(IV)	(V)	(VI)	Av.	(IV)	(V)	(VI)	Av.	(IV)	(V)	(VI)	Av.	theory
U_4O_9	75	13	12	4.37	79	20	1	4.21	51	49	0	4.49	4.50
U_3O_7	58	15	26	4.68	61	39	0	4.39	36	64	0	4.64	4.67
U_3O_8	0	41	59	5.59	0	88	12	5.12	0	65	35	5.35	5.33

[a]The average uranium valence derived from the experiments is compared to the theoretical value.

structure, this feature is clearly visible (see Figure 3). The crystallographic nature of ternary pentavalent uranium compounds influences heavily their U L_3-edge XANES spectrum. Notably in $TlUO_3$ which crystallizes in a defective pyrochlore structure, the white line position is shifted by ~3 eV as compared to KUO_3.[42,43] Obviously, such effects will highly influence the principal component analysis based on the shape and position of XANES spectra. If for these reasons the KUO_3 spectrum is excluded from the U L_3-edge XANES data set, different results on the distribution of valence states are obtained: U(IV) and U(V) chemical states are associated to U_4O_9 and U_3O_7, and a significant contribution of U(VI) appears only in U_3O_8 (see Table 2, middle columns). Qualitatively, this corresponds to the results derived from HERFD-XANES at the U M_4-edge, but considerable quantitative differences remain. The white line positions corresponding to the isolated U(IV)−U(V)−U(VI) components are shown in Figure 3, for illustration. Clearly, the U L_3-edge XANES data do not allow one to unambiguously determine the valence state distribution in mixed-valence compounds using the principal component analysis approach.

3.3. Local Structure in U(IV) and U(V) Environments. To assess the local structural evolution from UO_2 to U_3O_7, precise EXAFS data were extracted up to k values of 15 Å^{-1}. UO_2 and KUO_3 spectra were analyzed as reference for U(IV) and U(V) local environments. The symmetry restrictions applying to the most relevant (U−O) scattering paths were first evaluated as a function of the (U−U) nearest-neighbor distance, to serve as constraints in the EXAFS fitting process (elaborate calculations are provided in the Supporting Information). UO_2 adopts a fluorite $Fm\overline{3}m$ structure, here referred to with the subscript "f", in which U atoms are cubic-coordinated by O atoms (Figure 4). The distance between uranium atoms in the first coordination sphere $R(U−U)_f$ equals 3.87 Å at RT and is defined as

$$R(U-U)_f = \frac{\sqrt{2}}{2}a_f \tag{1}$$
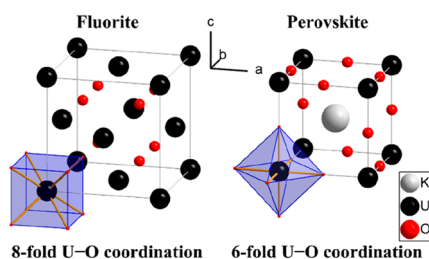
Figure 4. Illustration of cubic-coordinated (8-fold) and octahedrally coordinated (6-fold) uranium environments in the fluorite UO_2 and perovskite KUO_3 unit cells, respectively.

with a_f the lattice parameter of UO_2. The distance between uranium and oxygen atoms in the first coordination sphere $R(U−O)_f$ equals 2.37 Å at RT and is by symmetry restricted as

$$R(U-O)_f = \frac{\sqrt{3}}{4}a_f = \frac{\sqrt{3}}{2\sqrt{2}}R(U-U)_f \tag{2}$$

The length of the double scattering path $R(U−O−U)_f$ in UO_2 can be described as

$$R(U-O-U)_f = R(U-O)_f + \frac{1}{2}R(U-U)_f \tag{3}$$

$$R(U-O-U)_f = \frac{\sqrt{2}+\sqrt{3}}{4}a_f = \frac{\sqrt{2}+\sqrt{3}}{2\sqrt{2}}R(U-U)_f \tag{4}$$

and equals 4.30 Å at RT.

KUO_3 has a perovskite-type structure, in which U atoms are octahedrally coordinated by oxygen (Figure 4), here referred to with the subscript "ps". Evidently, the length of the (U−U) scattering path is directly related to the KUO_3 lattice parameter (a_{ps}):

$$R(U-U)_{ps} = a_{ps} \tag{5}$$

and equals 4.29 Å at RT. The oxygen atoms are positioned halfway on the unit cell axes and impose a simple symmetry restriction on the $R(U−O)_{ps}$ distance:

$$R(U-O)_{ps} = \frac{1}{2}a_{KUO3} = \frac{1}{2}R(U-U)_{ps} \tag{6}$$

equaling 2.37 Å at RT. The magnitude of the double scattering path $R(U−O−U)_{ps}$ is expressed simply as

$$R(U-O-U)_{ps} = R(U-U)_{ps} \tag{7}$$

In KUO_3, the U atoms are additionally cubic-coordinated by K atoms. The distance $R(U−K)_{ps}$ is subsequently described by

$$R(U-K)_{ps} = \frac{\sqrt{3}}{2}a_{ps} = \frac{\sqrt{3}}{2}R(U-U)_{ps} \tag{8}$$

and equals 3.72 Å at RT.

The UO_2 EXAFS data were fitted assuming two shells and one double scattering path, i.e., $R(U−O)_f$, $R(U−U)_f$, and $R(U−O−U)_f$. Similarly, the KUO_3 EXAFS data were fitted assuming three shells and one double scattering path, i.e., $R(U−O)_{ps}$, $R(U−K)_{ps}$, $R(U−U)_{ps}$, and $R(U−O−U)_{ps}$. The scattering factor (S_0^2) and the shift in threshold energy (ΔE_0) were refined as global parameters. The shift in the path-length (Δr) of each individual scattering path was constrained to the derived symmetry restrictions (eqs 1−8). Only the shift of the $R(U−U)$ path was chosen as a floating variable, to be interpreted as a measure for thermal contraction of the lattice. Debye−Waller factors (σ^2) of the single scattering paths were additionally refined, but in case of the double scattering path,

the parameter was constrained to the sum of both $R(U-O)$ and $R(U-U)$ paths. This results in five and six independent variables for the EXAFS fit of UO_2 and KUO_3, respectively.

The EXAFS spectra of UO_2 and KUO_3, and the corresponding fit to the data, are presented in Figure 5.
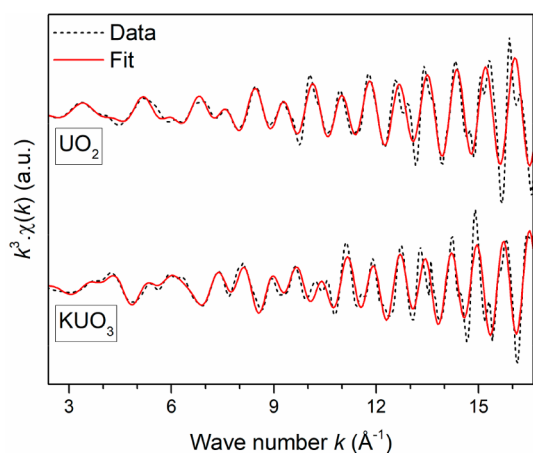
Figure 5. Experimental k^3-weighted EXAFS spectra (dashed line) of UO_2 and KUO_3, measured at the U L_3-edge in a helium cryostat (T = 18 K). Fits to the data based on the respective crystal structure of the compounds are displayed with a solid line.

Fourier transform (FT) moduli (magnitude and contribution of individual paths) of the respective data sets are presented in Figure 6. In UO_2, the data present two main features associated with the (U−O) and (U−U) coordination spheres, distributed
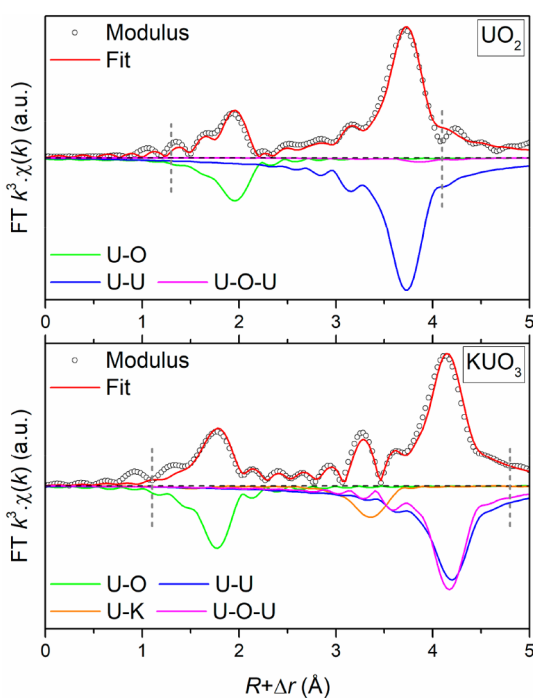
Figure 6. Fourier transform modulus of the EXAFS data corresponding with each compound (circles). The fit to the data is displayed with a solid red line, and the contribution of each individual path is shown by solid colored lines (mirrored to the x-axis to improve readability). Vertical dashed lines indicate the considered R-range.

around respectively 2.0 and 3.7 Å in the FT spectrum. The contribution of the double scattering path (U−O−U) is almost negligible. In general, the fit to the data is excellent, showing the validity of the structural model. An overview of the derived parameters is given in Table 3. The $R(U-O)$ distance

Table 3. Results Obtained after U L_3-edge EXAFS Refinement, Based on the Structural Information and Symmetry Restrictions Derived for UO_2 and KUO_3

	UO_2	KUO_3
R-factor	0.0176	0.0260
S_0^2	0.89(8)	0.92(7)
ΔE_0	4.1(6)	6.8(5)
$R(U-O)$ (Å)	2.368(3)	2.165(4)
σ^2 (Å^2)	0.003(1)	0.003(1)
$R(U-K)$ (Å)		3.750(6)
σ^2 (Å^2)		0.005(1)
$R(U-U)$ (Å)	3.867(4)	4.330(7)
σ^2 (Å^2)	0.0013(3)	0.0002(3)
(U−O−U) (Å)	4.301(4)	4.330(7)
σ^2 (Å^2)	0.005(1)	0.003(1)

associated with the U(IV) environment in UO_2 equals 2.368(3) Å under the applied conditions (T = 18 K). The corresponding lattice parameter equals 5.469(6) Å, based on the $R(U-U)$ value of 3.867(4) Å.

The FT spectrum of KUO_3 presents the same two features as observed in UO_2, associated with (U−O) and (U−U), but occurring at different distances (around 1.8 and 4.2 Å, respectively) because of its perovskite-type structure. Additionally, the (U−K) scattering path can be observed around 3.5 Å, and the contribution of the double scattering path (U−O−U) around 4.1 Å appears much more pronounced. The fit to the data is very good, although a slight deviation occurs in the very short distance region between 1.1 and 1.5 Å. This deviation is usually the consequence of the double-electronic excitation observed at actinide L_3-edges as reported by Hennig[44] and has no significant impact on the derived structural parameters. The results are given in Table 3 and show that the U(V) environment in KUO_3 is characterized by (U−O) and (U−K) coordination at 2.165(4) and 3.750(6) Å, respectively (at T = 18 K). The $R(U-U)$ distance of 4.330(7) Å defines also the cubic lattice parameter (T = 18 K) of the KUO_3 phase.

3.4. Assessment of the U_3O_7 Local Structure. The crystal structure of the U_3O_7 phase was for a long time not fully understood, but recently important breakthroughs were achieved.[13,16,17] It was demonstrated that the U_3O_7 phase consists of a fluorite parent arrangement of U and O atoms similar to UO_2 and that the excess oxygen induces local perturbations of the anion sublattice, resulting in a tetragonal deformation of the formerly cubic structure. Symmetry relations to the fluorite configuration in UO_2 impose a reduction of point group symmetry from $m3m$ to $4/mmm$, which allows one to derive the parent structure of U_3O_7.[16] Table 4 summarizes the fluorite parent arrangement of U and O atoms in U_3O_7 when, for simplicity, no occupancy associated with excess oxygen atoms is considered.

The most relevant (U−O) scattering paths in the tetragonal U_3O_7 parent structure (denoted here with the subscript "p") were evaluated similarly to the procedure outlined for UO_2 (elaborate calculations are provided in the Supporting

Table 4. Parent Structure Configuration of U and O Atoms in U_3O_7 (SG $P4_2/nnm$, Origin Choice 2), Here Disregarding Perturbations Caused by the Incorporation of Excess Oxygen

Wyckoff sites		x	y	z
U1	4f	0	0	0
O1	2a	1/4	3/4	1/4
O2	2b	3/4	1/4	1/4
O3	4c	1/4	1/4	1/4

Information). The nearest-neighbor $R(U–U_1)_p$ distance equals 3.80 Å at RT, but because of tetragonal symmetry, a second-nearest-neighbor $R(U–U_2)_p$ distance around 3.86 Å at RT can be identified. The uranium–uranium interatomic distances relate to the parent structure lattice parameters a_p (= 5.3793 Å) and c_p (= 5.5522 Å) as follows:

$$R(U–U_1)_p = \frac{\sqrt{2}}{2}a_p \tag{9}$$

and

$$R(U–U_2)_p = \frac{1}{2}\sqrt{a_p^2 + c_p^2} \tag{10}$$

The distance between uranium and oxygen atoms in the first coordination sphere $R(U–O)_p$, assuming a fluorite-type configuration, is then by symmetry restricted as

$$R(U–O)_p = \frac{1}{2}\sqrt{\frac{1}{2}a_p^2 + \frac{1}{4}c_p^2}$$
$$= \frac{1}{2}\sqrt{\frac{1}{2}R(U–U_1)_p^2 + R(U–U_2)_p^2} \tag{11}$$

Similar to the case of UO_2 described above, double scattering paths can be identified in U_3O_7. A formal description will be left out here because it could be shown that the contribution of these paths to the EXAFS signal was insignificant.

The U_3O_7 EXAFS data were fitted according to the parent structure model, assuming three single scattering paths, i.e., $R(U–O)_p$, $R(U–U_1)_p$, $R(U–U_2)_p$, and one double scattering path $R(U–O–U)_p$. The purpose of this approach is to understand the contribution of the parent configuration to the EXAFS, and hence, to illustrate the role the excess oxygen atoms must have on the structure. The shifts in the path-length (Δr) related to both $R(U–U_1)_p$ and $R(U–U_2)_p$ were chosen as a floating variable and interpreted as a measure for thermal contraction of the lattice. All other path lengths were constrained to the derived symmetry restrictions (eq 9−11). The followed methodology regarding refinement of scattering factor (S_0^2), shift in threshold energy (ΔE_0), and Debye−Waller factors (σ^2) was identical to the approach outlined earlier for UO_2 and KUO_3. For U_3O_7, seven variables were refined in the EXAFS fit.

The EXAFS spectrum of U_3O_7 and the corresponding parent structure fit of the data, as well as the derived FT moduli, are shown in the top part of Figures 7 and 8, respectively. The feature visible between 0.9−1.3 Å occurs outside of the R-range available for interpretation based on the data reduction method. Such an artifact is caused by double-electronic excitation,[44] and hence, it was not considered in the EXAFS evaluation. The $(U–U_1)$ and $(U–U_2)$ coordination spheres can be distinguished around 3.0 and 3.7 Å in the FT spectrum, whereas the $(U–O)$ contribution is attributed to multiple
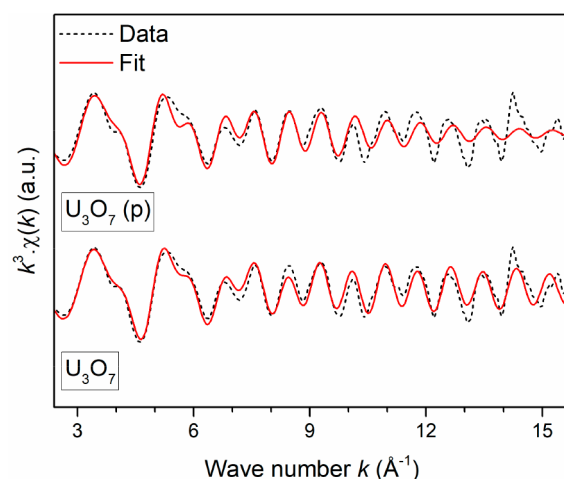
Figure 7. Experimental k^3-weighted EXAFS spectra (dashed line) of U_3O_7, measured at the U L_3-edge in a helium cryostat (T = 18 K). Fits to the data based on either the parent structure model (top) or the superstructure model (bottom) are displayed with a solid line.
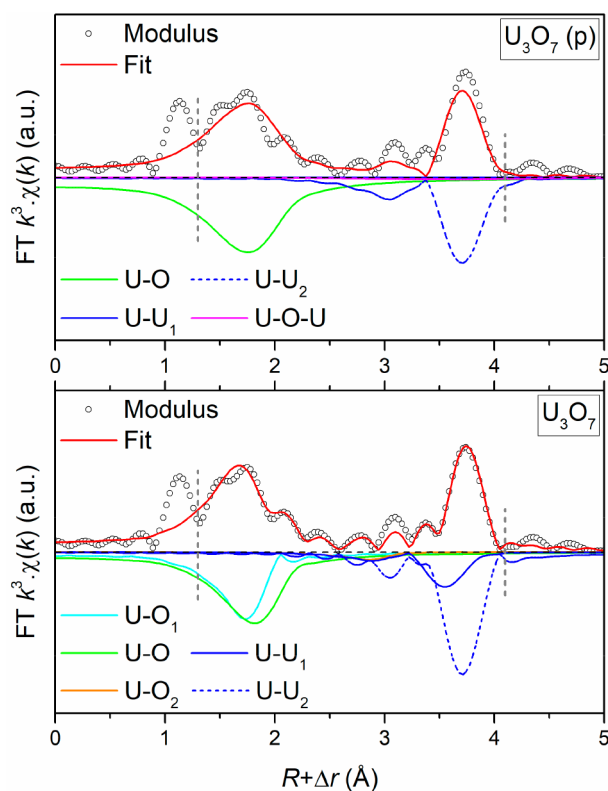
Figure 8. Fourier transform modulus of the U_3O_7 EXAFS data (circles). The fit to the data is displayed with a solid red line, and the contribution of each individual path is shown by solid colored lines (mirrored to the x-axis to improve readability). Vertical dashed lines indicate the considered R-range. The fit was based on the parent structure model (top) and on the average superstructure model (bottom). References to the different scattering paths are explained in the text.

features occurring in the short-range of the FT spectrum. The contribution of the double scattering path $(U–O–U)$ is negligible. The fit to the data is not good, indicating that the structural model needs to be adapted to take into account the perturbations caused by the excess oxygen atoms.

The U_3O_7 structural model derived recently from XRD and electron diffraction measurements is based on the tetragonal parent structure and considers a long-range ordering scheme of cuboctahedral oxygen clusters.[16] The relative size of the cluster depends on the value u (see introduction), and based on early neutron diffraction work u = 0.41 was suggested in the case of U_3O_7.[17] The occurrence of cuboctahedral oxygen clusters extends the uranium−oxygen interatomic distance profile to a range of values between 2.2 and 3.3 Å, assuming a regular geometry of the cuboctahedra. A histogram summarizing the total cumulative number of bonds binned per U−O distance in the $U_{60}O_{140}$ superstructure is available in the Supporting Information. On the basis of this structural model, four unique uranium coordination environments can be distinguished; see Figure 9. The anion configuration is composed of lattice
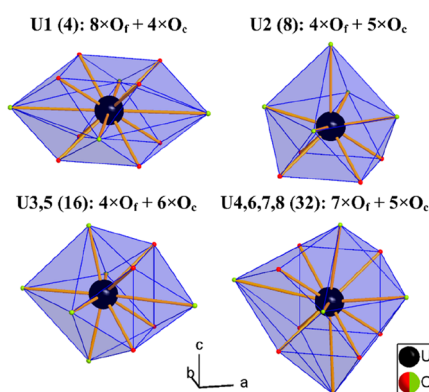
Figure 9. Illustration of the different uranium coordination environments in U_3O_7. The header of each polyhedron refers to the Wyckoff sites and multiplicity (in parentheses) as reported in ref 16. The origin of the neighboring oxygen atoms is abbreviated as O_f (fluorite-type) and O_c (cuboctahedral-type).

positions corresponding both to fluorite-type (red color) and cuboctahedral atomic sites (green color), thus increasing the uranium coordination from 8-fold to up to 12-fold.

It is now possible to define the relative occurrence of the various interatomic distances in a so-called average unit cell, by taking into account the atomic site multiplicities from the structural model. A histogram summarizing the average U−O coordination in U_3O_7 is presented in Figure 10. One can
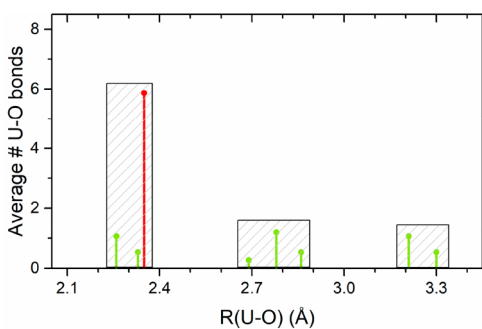
Figure 10. Histogram showing the occurrence and distribution of U−O bonds in an average unit cell of the U_3O_7 structural model at RT. Fluorite-type anion coordination (indicated in red) represent the largest fraction, situated at ∼2.35 Å. The occurrence of oxygen cuboctahedra results in additional U−O bonds (indicated in green) situated at short (∼2.25 Å), medium (∼2.80 Å), and long (∼3.25 Å) distances. The average coordination number equals 11.

distinguish a distribution into three separate regions situated around 2.3, 2.8, and 3.2 Å. The U−O coordination is on average 11-fold, with the largest fraction (∼6) being represented by the fluorite-type U−O bonds (indicated in red). The true distribution, however, depends on the relative size of the oxygen cuboctahedra, and their shape (i.e., deviation from regular into more distorted geometry), which needs to be evaluated from experimental data.

The information contained in the U_3O_7 EXAFS scattering data can be interpreted as a weighted-average of the different uranium environments. To investigate the local structure evolution from the input structural model, ideally all possible U−O scattering paths are considered in the EXAFS refinement. However, this results in a high correlation between the individual variables and overfitting of the data. Therefore, on the basis of the analysis of the histogram, we expanded the input model used in the parent structure refinement to include two generic U−O scattering paths at medium (∼2.80 Å) and long (∼3.25 Å) distances, in addition to the U−O scattering path at fluorite-type (∼2.35 Å) distance. The path length of fluorite-type bonds, denoted as $R(U-O)$, was restricted by symmetry according to eq 11, while those of the additional anion shells (denoted $R(U-O_1)$ and $R(U-O_2)$, respectively) were set as floating variables. To allow refinement of coordination numbers (N), the scattering factor was set fixed to 0.9, which corresponds to the value found for the UO_2 and KUO_3 EXAFS (Table 3). The sum of the coordination numbers was constrained to 11 to correspond with the value derived for the average unit cell.

The refinement converged well, and when including also the U−U scattering paths, Debye−Waller factors and the shift in threshold energy as outlined earlier (12 independent variables in total), a consistent agreement between the fit and experimental data was obtained (see bottom parts of Figures 7 and 8). Clearly, the agreement improves drastically by modeling the excess oxygen atoms in additional U−O scattering paths. The profile of the FT spectrum in the short-range (1.3−2.3 Å) is much better reproduced, although the two distinct features do not appear entirely deconvoluted. All features visible in the medium and long-range (2.3−4.0 Å) are correctly distinguished, with only a small misfit in intensity occurring around 3.1 Å.

The EXAFS refinement results of the simple parent structure and average superstructure model of U_3O_7 are reported in Table 5. The σ^2 values are reduced significantly; however, they remain elevated as compared to those observed in UO_2 and KUO_3. Furthermore, we observe that the U−O_1 path originally assumed to occur around 2.80 Å is refined to a much smaller value of 2.18 Å. The $R(U-U_1)$ and $R(U-U_2)$ values relate to the lattice parameters of the U_3O_7 phase, according to eqs 9 and 10, and equal to a_p = 5.23 (3) Å and c_p = 5.68 (5) Å at T = 18 K in the case of the average superstructure model. The uncertainty on these values is rather high, which can be understood because lattice parameters are per definition related to long-range periodicity, whereas the EXAFS is characteristic only of the local structure. The implications of all results are discussed in detail in section 4.

4. DISCUSSION

To probe the local structure in uranium compounds, EXAFS at the U L_3-edge is commonly applied. Spectra of phase-pure UO_2 and KUO_3 compounds were first analyzed to obtain information on the local structure of single-valence U(IV) and

Table 5. Results Obtained after U L_3-Edge EXAFS Refinement, Based on the Structural Information and Restrictions Defined for the U_3O_7 (p) Parent Structure, and the Average U_3O_7 Superstructure Model

	U_3O_7 (p)	U_3O_7
R-factor	0.1795	0.0339
S_0^2	1.3(2)	0.9[a]
ΔE_0	2(1)	0.7(6)
$R(U-O)$ (Å)	2.30(4)[c]	2.33(1)[c]
σ^2 (Å²)	0.020(4)	0.013(3)
N	8[a]	7.2(8)[b]
$R(U-O_1)$ (Å)		2.18(2)
σ^2 (Å²)		0.006(2)
N		2.7(5)[b]
$R(U-O_2)$ (Å)		3.33(5)
σ^2 (Å²)		0.01(1)
N		1.1(9)[b]
$R(U-U_1)$ (Å)	3.55(6)	3.70(2)
σ^2 (Å²)	0.32(1)	0.010(2)
N	4[a]	4[a]
$R(U-U_2)$ (Å)	3.85(2)	3.862(8)
σ^2 (Å²)	0.011(2)	0.006(1)
N	8[a]	8[a]

[a]Value restrained. [b]Sum of values constrained to 11. [c]Value constrained to symmetry operation.

U(V) environments. Recently, the crystallographic ordering in UO_2 has been questioned, especially at elevated temperatures, due to anomalous results obtained from pair-distribution functions of X-ray and neutron diffraction data.[45,46] The PDF appears to be better modeled by allowing distortion on the anion sublattice along <111> directions, i.e., implying a shift in the oxygen positions corresponding to $(1/4 + \delta, 1/4 + \delta, 1/4 + \delta)$ as described in space group $Pa\bar{3}$.[46] Interestingly, this can be seen to correspond also to the known anharmonic thermal vibrations which occur in the oxygen sublattice of UO_2.[47] This effect diminishes with temperature and is irrelevant at the experimental conditions applied in this study. Additionally, Prieur et al. found no evidence for deviation from the common fluorite structure in UO_2 in their recent EXAFS study performed at the U L_2-edge.[48] Therefore, the UO_2 EXAFS was modeled maintaining the original $Fm\bar{3}m$ crystal structure.

In U_3O_7, the atomic coordination is considerably more complex as compared to the single-valence compounds because multiple uranium environments exist. To gain more insight into the actual local structure, the EXAFS spectrum was refined based on an average representation of the U_3O_7 superstructure. When geometrically regular oxygen cuboctahedra are considered as defect clusters, four specific uranium environments can be defined (see Figure 9). In that case, the expected interatomic U–O distances are distributed in three main regions occurring around 2.3, 2.8, and 3.2 Å, respectively (see Figure 10). The results of the EXAFS fit, however, indicate that the U–O coordination occurs mainly at 2.18 (2), 2.33 (1), and 3.33 (5) Å, which is not entirely the same.

The histogram presented in Figure 10 refers to the interatomic distances derived from the structural model at room temperature (a_p = 5.38 Å and c_p = 5.55 Å). However, the EXAFS acquisition was performed at 18 K, and based on the fitted $R(U-U_1)$ and $R(U-U_2)$ values an anisotropic change in the lattice parameters occurred: a_p = 5.23 Å and c_p = 5.68 Å at T = 18 K. When these lattice parameters are applied on the

structural model, the distribution of U–O distances changes sensibly (see Figure 11). Consequently, the shortest U–O
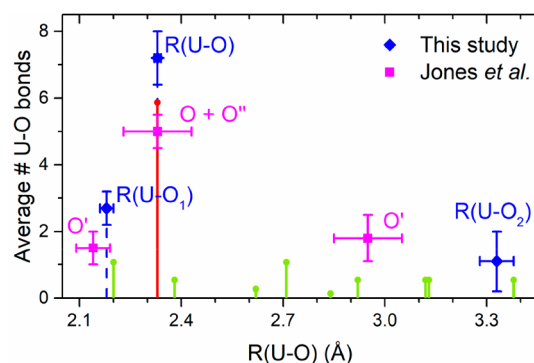
Figure 11. Histogram showing the occurrence and distribution of U–O bonds in an average unit cell of the U_3O_7 structural model (T = 18 K) and assuming a regular geometry of cuboctahedral oxygen clusters. Red and green color is used to differentiate between fluorite-type and additional U–O bonds, respectively. Current EXAFS results are displayed as blue diamonds, and results of Jones et al. are displayed as magenta squares.[21]

bond shifts to a value of 2.20 Å close to the obtained value for $R(U-O_1)$, while the $R(U-O)$ value remains aligned with the fluorite-type U–O bonds as imposed by the applied symmetry restriction. The remaining fraction of bonds occurs widely distributed at both medium and long interatomic distances, with $R(U-O_2)$ representing the contribution around 3.33 Å.

Our assessment of the U_3O_7 EXAFS can, at the moment, only be compared to the results of Jones et al.[21] Although they applied a difference Fourier technique to evaluate only the contribution of interstitial oxygen atoms, and did not take into account tetragonal symmetry, important similarities can be indicated (see Figure 11). In their analysis, the main contribution to the EXAFS relates to both fluorite and O″-type oxygen atoms at $R(U-O)$ = 2.33 (1) Å. The contribution of O′-type oxygen atoms, which constitute oxygen cuboctahedra, occurs at 2.14(5) and 3.0(1) Å. On the basis of these distances, the relative size of oxygen cuboctahedra would correspond to u = 0.37, in the notation applied throughout this work. We tried evaluating the EXAFS with an additional oxygen shell around 2.8 Å, but obtained a high correlation between the various parameters and negative Debye–Waller factors, which means we were at the limit of the EXAFS method.

A similar statement on the relative size of the oxygen cuboctahedra can be made, based on the U–O₁ and U–O₂ scattering paths refined from the EXAFS reported here. The interatomic distances corresponding to $R(U-O_1)$ and $R(U-O_2)$ all relate to coordination from a neighboring oxygen cluster and are thus defined by the value u and the unit cell lattice parameters. However, more than one unique U–O distance relates to u because of tetragonal symmetry in U_3O_7. This also explains why the profiles of individual U–O scattering paths appear broadened in the FT of the EXAFS (see Figure 8), which is expressed by σ^2 values considerably larger than those observed in UO_2 and KUO_3. Because the experimental acquisition was performed at T = 18 K, the large σ^2 values can be interpreted as a measure of disorder; i.e., the refined scattering paths actually represent a distribution of slightly differing interatomic distances. The most relevant

relations between $R(U-O_1)$ and $R(U-O_2)$ and u are worked out in the Supporting Information. We subsequently find that the cuboctahedral oxygen clusters are defined by $u = 0.40$ (1), based on the evaluation of the EXAFS data. This value is slightly larger than the value reported by Jones et al. ($u = 0.37$),[21] but in very good agreement with results ($u = 0.41$) obtained by Garrido et al. from early neutron diffraction work.[17]

A deviation from the regular geometry in the cuboctahedral oxygen clusters has been proposed from the analysis of selected-area electron diffraction (SAED) patterns, reported earlier.[16] Although the exact configuration (i.e., accurate atomic positions of the anions) could not be derived from the SAED patterns, one particular example was worked out based on a bond-valence sum evaluation in that study. One uranium site (i.e., U6, representing 8 out of 60 U atoms) was associated with a U(VI) environment due to the occurrence of uranyl-type U–O bonds (1.97 Å), while maintaining an average uranium valence of 4.67 as required by theory. However, in the present EXAFS evaluation, the very short interatomic distances associated with a U(VI) character were not reproduced, which indicates that the geometry of the cuboctahedral oxygen clusters needs to be re-evaluated. Our results support the latest insights obtained from experiments and calculations, which agree on the occurrence of only U(IV) and U(V) environments in U_3O_7,[27,28] thus solving the ambiguity concerning the valence state determination.[25,26]

The broad distribution of interatomic distances occurring in the U_3O_7 structural model relates not only to the size and shape of the cuboctahedral oxygen clusters, but also to the occupation of fluorite-type anion sites. Considering the high σ^2 value associated with the $R(U-O)$ scattering path, the fluorite-type anion sites are expected to be shifted from the parent structure positions. In general, the exact configuration of the entire anion sublattice in the $U_{60}O_{140}$ structural model can give rise to up to eight different uranium environments. This strongly complicates the interpretation of the *average* local structure probed by EXAFS. In order to complete the structural model, a quantitative evaluation of diffraction data sensitive to the contribution of oxygen atoms (e.g., neutron diffraction) is indispensable. This will allow us to better understand the structural changes induced by the oxidation of UO_2 into U_3O_7, and ultimately, U_3O_8.

5. CONCLUSION

In the current work, a comprehensive analysis of X-ray absorption data obtained at the U L_3-edge for various uranium compounds is reported. The focus has been to evaluate the uranium valence state and to assess the U_3O_7 local structure by means of HERFD-XANES and EXAFS methods.

The valence distribution in U_3O_7, and other mixed-valence uranium compounds, cannot be unambiguously quantified from XANES data at the U L_3-edge. The chemical shifts are around 2.4 eV, whereas the spectral line broadening of both conventional XANES ($\sim$8.8 eV) and of the HERFD-XANES method ($\sim$3.9 eV) is sensibly higher. Our recommendation is to refer to U $M_{4,5}$-edge HERFD-XANES for the accurate assessment of uranium chemical states, based on the following reasons: (1) The total energy broadening at the U M_4-edge is smaller ($\sim$0.7 eV) than the expected chemical shifts ($\sim$1.5 eV).[2,25] (2) According to the dipole selection rules, XANES spectra at the U L_3-edge contain information on the unoccupied U 6d states, whereas the uranium valence is

associated more to the U 5f states (which are effectively probed at the U $M_{4,5}$ absorption edges). (3) Unlike the more localized character of 5f states, U 6d states participate in hybridization with ligands, and hence, the L_3-edge is affected strongly by crystal field effects. As a result, U L_3-edge XANES spectra of uranate compounds, used often as single-valence references, cannot be confidently used in principal component analyses. We show that the qualitative distribution of U(IV) and U(V) in U_4O_9 and U_3O_7, and U(V) and U(VI) in U_3O_8, as reported earlier,[25] can be reproduced only when the KUO_3 spectrum is disregarded as a U(V) reference.

The U_3O_7 sample investigated in this work was fabricated by means of a controlled, nonambient XRD measurement. The onset of the tetragonal distortion upon oxidation of UO_2 could be clearly followed, and a phase-pure sample displaying a stable c/a ratio of 1.032 was obtained. The local structure assessment by means of EXAFS was based on an average model of the $U_{60}O_{140}$ superstructure, which allowed us to investigate the influence of excess oxygen atoms on the fluorite parent structure. The main contributions to the EXAFS, apart from U–U coordination, originates from interatomic U–O distances at 2.18 (2), 2.33 (1), and 3.33 (5) Å. The U–O coordination can be interpreted by the spatial arrangement of cuboctahedral oxygen clusters, with an average size denoted by the parameter $u = 0.40$ (1). The distorted configuration proposed from the analysis of SAED patterns needs to be re-evaluated[16] because the observed interatomic distances do not suggest any environment associated with a formal U(VI) valence.

ASSOCIATED CONTENT

Supporting Information

The Supporting Information is available free of charge at https://pubs.acs.org/doi/10.1021/acs.inorgchem.9b03702.

> Details on symmetry restrictions applying to the most relevant EXAFS scattering paths. Histogram showing the total cumulative number of U–O bonds in $U_{60}O_{140}$. Overview of relations between interatomic U–O distances and the parameter u (PDF)

AUTHOR INFORMATION

Corresponding Author

Gregory Leinders − *Belgian Nuclear Research Centre (SCK CEN), Institute for Nuclear Materials Science, B-2400 Mol, Belgium;* ⓞ orcid.org/0000-0001-6828-8248; Phone: +32 14 33 31 63; Email: gregory.leinders@sckcen.be

Authors

René Bes − *Department of Applied Physics and Helsinki Institute of Physics, Department of Applied Physics, Aalto University, FI-00076 Aalto, Finland;* ⓞ orcid.org/0000-0003-4206-1525

Kristina O. Kvashnina − *The Rossendorf Beamline at ESRF − The European Synchrotron, 38043 Grenoble, France; Helmholtz-Zentrum Dresden-Rossendorf (HZDR), Institute of Resource Ecology, 01314 Dresden, Germany*

Marc Verwerft − *Belgian Nuclear Research Centre (SCK CEN), Institute for Nuclear Materials Science, B-2400 Mol, Belgium*

Complete contact information is available at:
https://pubs.acs.org/10.1021/acs.inorgchem.9b03702

Notes

The authors declare no competing financial interest.

■ REFERENCES

(1) Cotton, S. *Lanthanide and Actinide Chemistry*; Wiley: Chichester, 2006.

(2) Kvashnina, K. O.; Butorin, S. M.; Martin, P.; Glatzel, P. Chemical state of complex uranium oxides. *Phys. Rev. Lett.* **2013**, *111*, 253002.

(3) Andersson, D. A.; Baldinozzi, G.; Desgranges, L.; Conradson, D. R.; Conradson, S. D. Density functional theory calculations of UO_2 oxidation: Evolution of UO_{2+x}, U_4O_{9-y}, U_3O_7, and U_3O_8. *Inorg. Chem.* **2013**, *52*, 2769−2778.

(4) Conradson, S. D.; Manara, D.; Wastin, F.; Clark, D. L.; Lander, G. H.; Morales, L. A.; Rebizant, J.; Rondinella, V. V. Local Structure and Charge Distribution in the UO2-U4O9 System. *Inorg. Chem.* **2004**, *43*, 6922−6935.

(5) Chevalier, P. Y.; Fischer, E.; Cheynet, B. Progress in the thermodynamic modelling of the O-U binary system. *J. Nucl. Mater.* **2002**, *303*, 1−28.

(6) Labroche, D.; Dugne, O.; Chatillon, C. Thermodynamic properties of the O-U system. II - Critical assessment of the stability and composition range of the oxides UO_{2+x}, U_4O_{9-y} and U_3O_{8-z}. *J. Nucl. Mater.* **2003**, *312*, 50−66.

(7) Higgs, J. D.; Lewis, B. J.; Thompson, W. T.; He, Z. A conceptual model for the fuel oxidation of defective fuel. *J. Nucl. Mater.* **2007**, *366*, 99−128.

(8) Guéneau, C.; Dupin, N.; Sundman, B.; Martial, C.; Dumas, J.-C.; Gossé, S.; Chatain, S.; Bruycker, F. D.; Manara, D.; Konings, R. J. M. Thermodynamic modelling of advanced oxide and carbide nuclear fuels: Description of the U-Pu-O-C systems. *J. Nucl. Mater.* **2011**, *419*, 145−167.

(9) Abe, T., Asakura, K. 2.15 - Uranium Oxide and MOX Production. In *Comprehensive Nuclear Materials*; Elsevier: Oxford, 2012; pp 393−422.

(10) Shoesmith, D. W. Fuel corrosion processes under waste disposal conditions. *J. Nucl. Mater.* **2000**, *282*, 1−31.

(11) Poulesquen, A.; Desgranges, L.; Ferry, C. An improved model to evaluate the oxidation kinetics of uranium dioxide during dry storage. *J. Nucl. Mater.* **2007**, *362*, 402−410.

(12) Leinders, G.; Pakarinen, J.; Delville, R.; Cardinaels, T.; Binnemans, K.; Verwerft, M. Low-temperature oxidation of fine UO_2 powders: A process of nanosized domain development. *Inorg. Chem.* **2016**, *55*, 3915−3927.

(13) Desgranges, L.; Baldinozzi, G.; Rousseau, G.; Nièpce, J.-C.; Calvarin, G. Neutron diffraction study of the in situ oxidation of UO_2. *Inorg. Chem.* **2009**, *48*, 7585−7592.

(14) Bevan, D. J. M.; Grey, I. E.; Willis, B. T. M. The crystal structure of β-U_4O_{9-y}. *J. Solid State Chem.* **1986**, *61*, 1−7.

(15) Rousseau, G.; Desgranges, L.; Charlot, F.; Millot, N.; Nièpce, J. C.; Pijolat, M.; Valdivieso, F.; Baldinozzi, G.; Bérar, J. F. A detailed study of UO_2 to U_3O_8 oxidation phases and the associated rate-limiting steps. *J. Nucl. Mater.* **2006**, *355*, 10−20.

(16) Leinders, G.; Delville, R.; Pakarinen, J.; Cardinaels, T.; Binnemans, K.; Verwerft, M. Assessment of the U_3O_7 Crystal Structure by X-ray and Electron Diffraction. *Inorg. Chem.* **2016**, *55*, 9923−9936.

(17) Garrido, F.; Ibberson, R. M.; Nowicki, L.; Willis, B. T. M. Cuboctahedral oxygen clusters in U_3O_7. *J. Nucl. Mater.* **2003**, *322*, 87−89.

(18) Jolibois, P. A new oxide of uranium, U_3O_7. *C.R. Acad. Sci.* **1947**, *224*, 1395−1396.

(19) Brincat, N. A.; Molinari, M.; Allen, G. C.; Storr, M. T.; Parker, S. C. Density functional theory calculations of defective UO_2 at U_3O_7 stoichiometry. *J. Nucl. Mater.* **2015**, *467*, 724−729.

(20) Nowicki, L.; Garrido, F.; Turos, A.; Thomé, L. Polytypic arrangements of cuboctahedral oxygen clusters in U_3O_7. *J. Phys. Chem. Solids* **2000**, *61*, 1789−1804.

(21) Jones, D. J.; Roziere, J.; Allen, G. C.; Tempest, P. A. The structural determination of fluorite-type oxygen excess uranium oxides using EXAFS spectroscopy. *J. Chem. Phys.* **1986**, *84*, 6075−6082.

(22) Allen, G. C.; Tempest, P. A.; Garner, C. D.; Ross, I.; Jones, D. J. EXAFS: a new approach to the structure of uranium oxides. *J. Phys. Chem.* **1985**, *89*, 1334−1336.

(23) Willis, B. T. M. Point defects in uranium oxides. *Proc. Br. Ceram. Soc.* **1964**, No. 1, 9−19.

(24) Cooper, R. I.; Willis, B. T. M. Refinement of the structure of β-U_4O_9. *Acta Crystallogr., Sect. A: Found. Crystallogr.* **2004**, *60*, 322−325.

(25) Leinders, G.; Bes, R.; Pakarinen, J.; Kvashnina, K.; Verwerft, M. Evolution of the Uranium Chemical State in Mixed-Valence Oxides. *Inorg. Chem.* **2017**, *56*, 6784−6787.

(26) Sanyal, K.; Khooha, A.; Das, G.; Tiwari, M. K.; Misra, N. L. Direct Determination of Oxidation States of Uranium in Mixed-Valent Uranium Oxides Using Total Reflection X-ray Fluorescence X-ray Absorption Near-Edge Spectroscopy. *Anal. Chem.* **2017**, *89*, 871−876.

(27) Wang, X.; Qiu, R.-Z.; Long, Z.; Lu, L.; Hu, Y.; Liu, K.-Z.; Zhang, P.-C. Chemical State of U in U−N−O Ternary System from First-Principles Calculations. *J. Phys. Chem. C* **2019**, *123*, 17155.

(28) Kvashnina, K. O.; Kowalski, P. M.; Butorin, S. M.; Leinders, G.; Pakarinen, J.; Bès, R.; Li, H.; Verwerft, M. Trends in the valence band electronic structures of mixed uranium oxides. *Chem. Commun.* **2018**, *54*, 9757−9760.

(29) Leinders, G.; Cardinaels, T.; Binnemans, K.; Verwerft, M. Accurate lattice parameter measurements of stoichiometric uranium dioxide. *J. Nucl. Mater.* **2015**, *459*, 135−142.

(30) Leinders, G.; Cardinaels, T.; Binnemans, K.; Verwerft, M. Low-Temperature Oxidation of Fine UO_2 Powders: Thermochemistry and Kinetics. *Inorg. Chem.* **2018**, *57*, 4196−4204.

(31) Hölzer, G.; Fritsch, M.; Deutsch, M.; Härtwig, J.; Förster, E. $K\alpha_{1,2}$ and $K\beta_{1,3}$ X-ray emission lines of the 3d transition metals. *Phys. Rev. A: At., Mol., Opt. Phys.* **1997**, *56*, 4554−4568.

(32) Rovezzi, M.; Lapras, C.; Manceau, A.; Glatzel, P.; Verbeni, R. High energy-resolution x-ray spectroscopy at ultra-high dilution with spherically bent crystal analyzers of 0.5 m radius. *Rev. Sci. Instrum.* **2017**, *88*, 013108.

(33) Kvashnina, K. O.; Scheinost, A. C. A Johann-type X-ray emission spectrometer at the Rossendorf beamline. *J. Synchrotron Radiat.* **2016**, *23*, 836−841.

(34) Kvashnina, K. O.; Kvashnin, Y. O.; Butorin, S. M. Role of resonant inelastic X-ray scattering in high-resolution core-level spectroscopy of actinide materials. *J. Electron Spectrosc. Relat. Phenom.* **2014**, *194*, 27−36.

(35) Ravel, B.; Newville, M. ATHENA, ARTEMIS, HEPHAESTUS: data analysis for X-ray absorption spectroscopy using IFEFFIT. *J. Synchrotron Radiat.* **2005**, *12*, 537−541.

(36) Newville, M. IFEFFIT: interactive XAFS analysis and FEFF fitting. *J. Synchrotron Radiat.* **2001**, *8*, 322−324.

(37) Soldatov, A. V.; Lamoen, D.; Konstantinovic, M. J.; Van den Berghe, S.; Scheinost, A. C.; Verwerft, M. Local structure and oxidation state of uranium in some ternary oxides: X-ray absorption analysis. *J. Solid State Chem.* **2007**, *180*, 54−61.

(38) Rossberg, A.; Ulrich, K.-U.; Weiss, S.; Tsushima, S.; Hiemstra, T.; Scheinost, A. C. Identification of Uranyl Surface Complexes on Ferrihydrite: Advanced EXAFS Data Analysis and CD-MUSIC Modeling. *Environ. Sci. Technol.* **2009**, *43*, 1400−1406.

(39) Nelin, C. J.; Bagus, P. S.; Ilton, E. S. Theoretical analysis of the U L3-edge NEXAFS in U oxides. *RSC Adv.* **2014**, *4*, 7148−7153.

(40) Butorin, S. M.; Modin, A.; Vegelius, J. R.; Suzuki, M.-T.; Oppeneer, P. M.; Andersson, D. A.; Shuh, D. K. Local Symmetry Effects in Actinide 4f X-ray Absorption in Oxides. *Anal. Chem. (Washington, DC, U. S.)* **2016**, *88*, 4169−4173.

(41) Vitova, T.; Kvashnina, K. O.; Nocton, G.; Sukharina, G.; Denecke, M. A.; Butorin, S. M.; Mazzanti, M.; Caciuffo, R.; Soldatov, A.; Behrends, T.; Geckeis, H. High energy resolution x-ray absorption spectroscopy study of uranium in varying valence states. *Phys. Rev. B: Condens. Matter Mater. Phys.* **2010**, *82*, 235118.

(42) Misra, N. L.; Lahiri, D.; Mudher, K. D. S.; Olivi, L.; Sharma, S. M. XANES study on novel mixed valent $A_2U_4O_{12}$ (A = K, Rb or Tl) uranates. *X-Ray Spectrom.* **2008**, *37*, 215−218.

(43) Aravamudan, G.; Giridharan, A. S.; Ramadass, N. Thallium(I) Uranate(V). *Z. Anorg. Allg. Chem.* **1978**, *446*, 246−250.

(44) Hennig, C. Evidence for double-electron excitations in the L_3-edge x-ray absorption spectra of actinides. *Phys. Rev. B: Condens. Matter Mater. Phys.* **2007**, *75*, 035120.

(45) Skinner, L. B.; Benmore, C. J.; Weber, J. K. R.; Williamson, M. A.; Tamalonis, A.; Hebden, A.; Wiencek, T.; Alderman, O. L. G.; Guthrie, M.; Leibowitz, L.; Parise, J. B. Molten uranium dioxide structure and dynamics. *Science* **2014**, *346*, 984−987.

(46) Desgranges, L.; Ma, Y.; Garcia, P.; Baldinozzi, G.; Siméone, D.; Fischer, H. E. What Is the Actual Local Crystalline Structure of Uranium Dioxide, UO_2? A New Perspective for the Most Used Nuclear Fuel. *Inorg. Chem.* **2017**, *56*, 321−326.

(47) Barrett, N. T.; Greaves, G. N.; Willis, B. T. M.; Antonini, G. M.; Thornley, F. R. Anharmonic vibrations in UO_2 as determined by EXAFS. *J. Phys. C: Solid State Phys.* **1988**, *21*, L791−L796.

(48) Prieur, D.; Epifano, E.; Dardenne, K.; Rothe, J.; Hennig, C.; Scheinost, A. C.; Neuville, D. R.; Martin, P. M. Peculiar Thermal Behavior of UO_2 Local Stucture. *Inorg. Chem.* **2018**, *57*, 14890−14894.